Low-loss passive waveguides in a generic InP foundry process via local diffusion of zinc

Domenico D'Agostino,[1,*] **Giuseppe Carnicella,**[2] **Caterina Ciminelli,**[2]
Peter Thijs,[1] **Petrus J. Veldhoven,**[1,*] **Huub Ambrosius,**[1] **and Meint Smit**[1]

[1]*COBRA Research Institute, Eindhoven University of Technology, 5600 MB Eindhoven, The Netherlands*
[2]*Optoelectronics Laboratory, Politecnico di Bari, Via Orabona 4, 70125 Bari, Italy*
[*]d.dagostino@tue.nl

Abstract: Generic InP foundry processes allow monolithic integration of active and passive elements into a common p-n doped layerstack. The passive loss can be greatly reduced by restricting the p-dopant to active regions. We report on a localized Zn-diffusion process based on MOVPE, which allows to reduce waveguide loss from 2 dB/cm to below 0.4 dB/cm. We confirm this value by fabrication of a 73 mm long spiral ring resonator, with a record quality factor of 1.2 million and an extinction ratio of 9.7 dB.

References and links

1. R. Nagarajan, C. H. Joyner, R. P. Jr. Schneider, J. S. Bostak, T. Butrie, A. G. Dentai, V. G. Dominic, P. W. Evans, M. Kato, M. Kauffman, D. J. H. Lambert, S. K. Mathis, A. Mathur, R. H. Miles, M. L. Mitchell, M. J. Missey, S. Murthy, A. C. Nilsson, F. H. Peters, S. C. Pennypacker, J. L. Pleumeekers, R. A. Salvatore, R. K. Schlenker, R. B. Taylor, T. Huan-Shang, M. F. Van Leeuwen, J. Webjorn, M. Ziari, D. Perkins, J. Singh, S. G. Grubb, M. S. Reffle, D. G. Mehuys, F. A. Kish, and D. F. Welch, "Large-scale photonic integrated circuits," IEEE J. Sel. Top. in Quantum Electron, **11**(1), 50–65 (2005).
2. R. Stabile, A. Rohit, and K. A. Williams, "Wavelength selective cross-connect," J. Lightwave. Technol. **32**(2), 201–207 (2014).
3. C. Ciminelli, F. Dell'Olio, C. E. Campanella, and M.N. Armenise, "Photonic technologies for angular velocity sensing," Adv. Opt. Photonics **2**(3), 370 (2010).
4. C. Ciminelli, F. Dell'Olio, M. N. Armenise, F. M. Soares, and W. Passenberg, "High performance InP ring resonator for new generation monolithically integrated optical gyroscopes," Opt. Express **21**(1), 302–305 (2013).
5. N. Futakuchi, S. Xueliang, D. Miyashita, M. Kato, and Y. Nakano. "Fabrication of InGaAsP/InP Mach-Zehnder interferometer optical amplifier switches by metalorganic vapor phase selective area epitaxy," in *Proceedings of IEEE International Conference on Indium Phosphide and Related Materials* (IEEE, 2001), pp. 583-586
6. V. Tolstikhin, "Regrowth-Free Multi-Guide Vertical Integration in InP for Optical Communications Multi-guide vertical integration Building block approach," in *Proceedings of IEEE International Conference on Indium Phosphide and Related Materials* (IEEE, 2011), pp. 3-6.
7. J. Wallin, G. Landgren, K. Streubel, S. Nilsson, and M. Oberg. "Selective Area Regrowth of Butt-joint Coupled Waveguides in Multi-section DBR Lasers," in *Proceedings of IEEE Sixth International Conference on Metalorganic Vapor Phase Epitaxy* (IEEE, 1992), pp. 73–74.
8. M. K. Smit, X. J. M. Leijtens, H. P. M. M. Ambrosius, E. Bente, J. van der Tol, B. Smalbrugge, T. de Vries, E. J. Geluk, J. Bolk, R. van Veldhoven, L. Augustin, P. Thijs, D. D'Agostino, H. Rabbani, K. Lawniczuk, S. Stopinski, S. Tahvili, A. Corradi, E. Kleijn, D. Dzibrou, M. Felicetti, E. Bitincka, V. Moskalenko, J. Zhao, R. Santos, G. Gilardi, W. Yao, K. Williams, P. Stabile, P. Kuindersma, J. Pello, S. Bhat, Y. Jiao, D. Heiss, G. Roelkens, M. J. Wale, P. Firth, F.M. Soares, N. Grote, M. Schell, H. Debregeas, M. Achouche, J. L. Gentner, A. Bakker, T. Korthorst,

D. Gallagher, A. Dabbs, A. Melloni, F. Morichetti, D. Melati, A. Wonfor, R. Penty, R. Broeke, B. Musk, and D. Robbins, "An introduction to InP-based generic integration technology," Semicond. Sci. Technol. **29**, 083001 (2014).

9. E. Bitincka, G. Gilardi, and M. K. Smit, "On-wafer optical loss measurements using ring resonators with integrated sources and detectors," IEEE Photon. J. **6**(5), 1–12 (2014).

10. T. Touam, C. Wu, Y. Gigase, M. Belanger, J. F. Currie, and S. I. Najafi. "Fabrication, characterization, and analysis of zinc-diffused GaAs waveguides," IEEE J. Quantum Electron. **25**(5), 850–853 (1989).

11. M. H. Ettenberg, M. J. Lange, A. R. Sugg, M. J. Cohen, and G. H. Olsen, "Zinc diffusion in InAsP/InGaAs heterostructures," J. Electron. Mater. **28**, 1433–1439 (1999).

12. M. Wada, M. Seko, K. Sakakibara, and Y. Sekiguchi, "Zn diffusion into InP using dimethylzinc as a Zn source," Jpn. J. Appl. Phys. **28**, 1700–1703 (1989).

13. K. Vanhollebeke, M. D'Hondt, I. Moerman, P. Daele, and P. Demeester, "Zn doping of InP, InAsP/InP, and InAsP/InGaAs heterostructures through metalorganic vapor phase diffusion (MOVPD)," J. Electron. Mater. **30**(8), 951–959 (2001).

14. D. Franke, F.W. Reier, and N. Grote, "Post-growth Zn diffusion into InGaAs/InP in a LP-MOVPE reactor," J. Cryst. Growth, **195**(1-4), 112–116 (1998).

15. J. P. Weber, "Optimization of the carrier-induced effective index change in InGaAsP waveguides - application to tunable Bragg filters," IEEE J. Quantum Electron. **30**(8), 1801–1816 (1994).

16. W. Walukiewicz, J. Lagowski, L. Jastrzebski, P. Rava, M. Lichtensteiger, C. H. Gatos, and H. C. Gatos, "Electron mobility and free-carrier absorption in InP; determination of the compensation ratio," J. Appl. Phys. **51**(5), 2659 (1980).

17. F. P. Payne and J. P. R. Lacey, "A theoretical analysis of scattering loss from planar optical waveguides," Opt. Quant. Electron. **26**, 977–986 (1994).

18. K. P. Yap, A. Delage, J. Lapointe, B. Lamontagne, J.H. Schmid, Philip Waldron, B.A. Syrett, and S. Janz, "Correlation of scattering loss, sidewall roughness and waveguide width in Silicon-on-Insulator (SOI) ridge waveguides," J. Lightwave. Technol. **27**(18), 3999–4008 (2009).

19. A. Yamaguchi and O. Komuro, "Characterization of line edge roughness in resist patterns by using fourier analysis and auto-correlation function," Jpn. J. Appl. Phys. **42**, 3763–3770 (2003).

20. T. Feuchter and C. Thirstrup, "High precision planar waveguide propagation loss measurement technique using a Fabry-Perot cavity," IEEE Photon. Techn. Lett. **6**, 4–7 (1994).

21. W. Bogaerts, P. De Heyn, T. Van Vaerenbergh, K. De Vos, S. Kumar Selvaraja, T. Claes, P. Dumon, P. Bienstman, D. Van Thourhout, and R. Baets, "Silicon microring resonators," Laser & Photon. Rev. **6**(1), 47–73 (2012).

22. D. X. Xu, A. Densmore, P. Waldron, J. Lapointe, E. Post, A. Delâge, S. Janz, P. Cheben, J. Schmid and B. Lamontagne, "High bandwidth SOI photonic wire ring resonators using MMI couplers," Opt. Express **15**(6), 3149–3155 (2007).

23. C. Ciminelli, F. Dell'Olio, C. E. Campanella, and M. N. Armenise, "Numerical and experimental investigation of an optical high-Q spiral resonator gyroscope," in *Proceedings of IEEE International Conference on Transparent Optical Networks* (IEEE, 2012), pp. 1-4.

24. M. T Hill, X. J. M. Leijtens, G. D. Khoe, and M. K. Smit, "Optimizing Imbalance and Loss in 2x2 3-dB multimode interference couplers via access waveguide width," J. Lightwave. Technol. **21**(10), 2305–2313 (2003).

25. M. Bachmann, P. A. Besse, and H Melchior, "Overlapping-image multimode interference couplers with a reduced number of self-images for uniform and nonuniform power splitting," Appl. Opt. **34**(30), 6898–6910 (1995).

26. E. Bitincka, Emil Kleijn, and Meint K. Smit, "Accuracy analysis of the fabry-perot measurement method," in *Advanced Photonics 2013*, OSA Technical Digest Series (Optical Society of America, 2013), paper JT3A.10.

1. Introduction

The loss of passive waveguides is an important performance parameter of photonic integration platforms, especially for large scale photonic integrated circuits (PICs) [1, 2] and components as delay lines or resonators. The latter are relevant for demanding sensing applications as integrated optical gyroscopes, where waveguide loss limits the sensitivity [3]. Recent advances in InP fabrication technology allowed for ring resonators with a waveguide loss of 0.45 dB/cm [4] and a quality factor of one million, suitable for gyroscopes with sufficient sensitivity for tactical applications. However, monolithic integration of sources with passive circuitry typically increases the waveguide loss to a level which is unsuitable for the applications as described above. Therefore they are dependent on hybrid solutions, which limits their miniaturization.

The loss depends largely on the applied active-passive integration approach as e.g. quantum-well intermixing [5], twin guide integration [6] or butt-joint integration [7]. The latter is the standard in most InP foundry platforms [8] and allows the selective growth of active and pas-

sive sections. Therefore, it has the advantage that the cross-sections of the active and passive regions can be optimized independently. To keep the number of regrowth steps as small as possible, an identical doped waveguide structure is used for phase modulators and passive waveguides, which compromises their performance. A typical loss value for PICs fabricated with this method is 2 dB/cm to 3 dB/cm [9].

This work studies the attainable propagation loss by restricting the dopant to the active regions. The dopant is introduced locally into the cladding of the wafer by diffusion of Zinc (Zn), which allows for a clear separation between the doping profiles in different waveguide sections. Up to now, various implementations of Zn-diffusion in InP have been reported: by polymer/glass spin-on films [10], by sealed quartz [11], by ampoule [12] and by MOVPE based diffusion [13]. In this work, we rely on the latter as it features a high repeatability, excellent wafer uniformity and sufficiently high doping concentrations to provide a linear current-voltage characteristic [14].

The outline of this paper is as follows. We describe diffusion experiments and discuss their compatibility with current InP foundry integration schemes. Further, we propose waveguide test structures to quantify the waveguide loss in diffused and not-diffused regions. The first structure is an array of waveguides which is routed through diffused regions of increasing length. The measurements indicate that by localizing the dopant, a reduction in propagation loss from 2 dB/cm to 0.4 dB/cm is obtained. The low propagation loss is verified using a spiral ring resonator with an effective circumference of 73 mm and a multimode interference (MMI) device as coupling element. The ring shows a quality factor of 1.2 million, which is about 20% higher than the highest value reported so far in InP [4].

2. Simulations

A simulation model was used to estimate the attainable waveguide loss based on a Zn-diffusion process, using the COBRA generic waveguides [8] depicted in Fig. 1 as an example.

We shall consider two contributions to the waveguide loss, being scattering and free carrier absorption. The p-doped absorption is modeled with a model to account for intervalence band absorption [15], while n-type absorption is modeled by accounting for scattering introduced through electron-phonon and electron-ionized impurity interactions [16]. The waveguide sidewall scattering is estimated by using the approach of Payne and Lacey [17], modified with a scaling factor to take into account the etch depth of the waveguides [18]. The predictions of the model are based on sidewall roughness and correlation length. We obtained these values from critical dimension-scanning electron microscope (CD-SEM) images of waveguide sidewalls, using the autocorrelation procedure as described in [19]. With this approach we found 3.5 nm
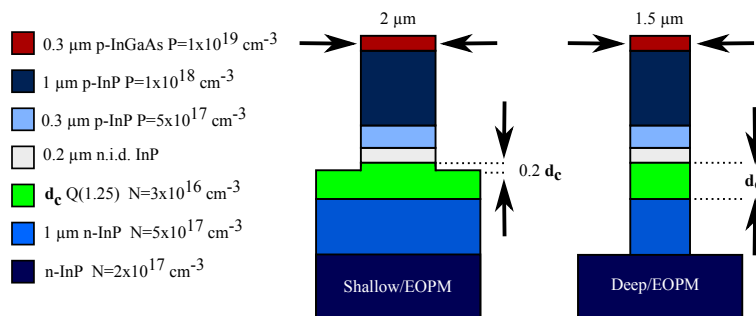

Fig. 1. Standard COBRA cross-sections used for phase modulators (EOPM) and passive waveguide fabrication. In the passive sections the 300 nm contact layer is removed to avoid bandgap absorption.

Table 1. Waveguide loss in dB/cm for waveguides with different core thickness and polarization, λ=1.55 μm.

| Core | N-Doped | | | | N and P-Doped | | | |
| | Shallow | | Deep | | Shallow | | Deep | |
	TE	TM	TE	TM	TE	TM	TE	TM
400 nm	0.54	0.61	1.39	1.26	3.20	4.31	4.60	5.38
500 nm	0.44	0.51	1.32	1.19	2.09	2.80	3.32	3.76
600 nm	0.37	0.44	1.28	1.14	1.43	1.91	2.59	2.83

roughness and a correlation length of 40 nm.

The models as described above, have been implemented into the 2D finite difference time domain (FDTD) mode simulator of Phoenix BV, to calculate the electric field profiles of the waveguides as presented in Fig. 1. For simulation purposes the etch depth of the shallow waveguide is parameterized, according to the thickness of the guiding layer d_c. The deep waveguides are assumed to be etched 400 nm below the core.

In order to study the different loss contributions, the waveguides are simulated both with and without the p-dopant in the top cladding. The simulated propagation loss is displayed in Table 1. The result suggests that loss can be kept below 0.6 dB/cm for a wide range of guiding layer thicknesses. The difference in loss between deep and shallow waveguides is attributed to the difference in scattering loss, which is estimated approximately as 1 dB/cm and 0.1 dB/cm respectively.

P-doped waveguides have a loss that is about one order of magnitude higher. Hence, the localization of the p-dopant to regions where electro-optical components are desired, can improve the waveguide performance greatly

3. Fabrication

3.1. Process flow

The diffusion process is designed to be integrated in existent standard foundry processes with minimal process adaptations. In Fig. 2, we give an example how diffusion is integrated into the current COBRA process flow [8], with just a few additional steps between epitaxy and waveguide fabrication.

The starting point is a layerstack with a non-intentionally doped (n.i.d.) cladding with an InGaAs top layer. Passive regions are protected with a dielectric hard-mask, in our case a 200
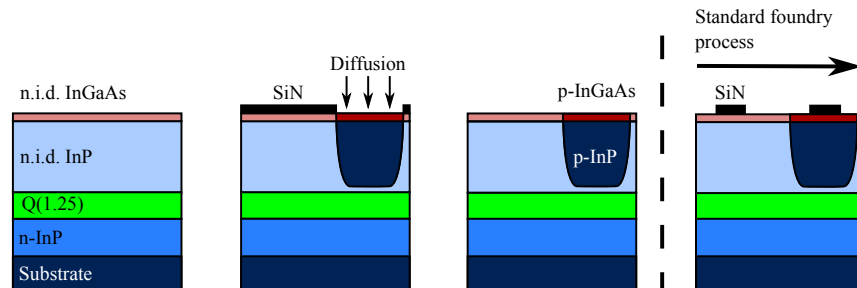
Fig. 2. Schematic diffusion process for the definition of localized p-n regions. Diffusion takes place in between epitaxy and waveguide fabrication.

nm thick Si_3N_4-layer. Using a MOVPE reactor, a diffusion process introduces Zn locally into the cladding. The diffusion of Zn into InP will result in a p-doped region with a depth that is proportional to the square-root of the diffusion time. If the diffusion depth can be controlled sufficiently accurate, the novel process is fully compatible with the standard waveguide process as it is presently used.

3.2. Diffusion experiments

Diffusion experiments were carried out to calibrate the diffusion depth. The experiments were performed on samples without masking, to allow for characterization of the diffusion profile with standard methods as capacitance voltage (CV) and secondary ion mass spectroscopy (SIMS) measurements. For the experiment, n-doped 2" InP wafers are overgrown with 2 μm n.i.d InP and 300 nm n.i.d InGaAs to simulate the cladding of the final layerstack. A Zn pressure of 0.0123 mBar was chosen and a temperature of 500 °C, while the time was varied up to 110 min. The measured diffusion profiles for five different times are shown in Fig. 3(a) for CV. The corresponding SIMS results for three out of those five samples are shown in Fig. 3(b).

Both figures show a drop in doping concentration, from approximately 1×10^{19} cm^{-3} to 1×10^{18} cm^{-3}, which coincides with the InGaAs/InP interface. The step height is related to the difference in solubility limit between InP and InGaAsP and agrees well with other experimental work based on MOVPE [13]. In InP the doping concentration is generally maintained above 5×10^{17} cm^{-3}, until a second drop indicates the diffusion front. The SIMS measurements are qualitatively similar to the ones obtained from CV, which suggests that most of the diffused Zn is electrically active. Furthermore, the doping concentrations, as specified for the COBRA platform, are indicated as dashed lines in Fig. 3(b) and show qualitatively good agreement with the diffusion profile.

The experiment has been repeated for a set of masked samples with 30 μm wide openings. The samples were cleaved to inspect the cross-section under the scanning electron microscope (SEM). A stain etch with K_4FeCN_6/KOH was performed to enhance material transitions. A typical SEM image is shown in Fig. 4. The bright area which is about 1.63 μm deep, indicates a change in conductivity related to the diffused p-dopant. We found that the diffusion depth
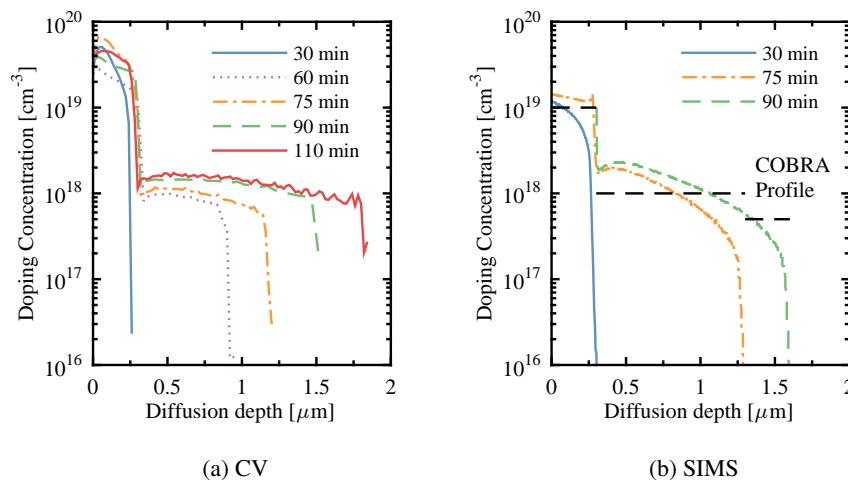

Fig. 3. Measured diffusion profiles for different exposure times. Dashed lines indicate the COBRA insitu target doping profile.
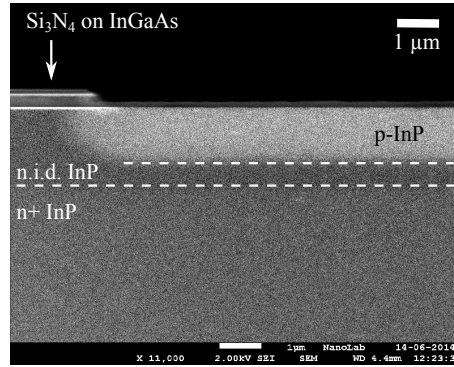
Fig. 4. SEM image of wafer crossection through a diffusion area.

measured by SEM is in good agreement with the result of CV and SIMS. We further recognize a lateral diffusion, which penetrates under the hard-mask and stops approximately after 800 nm. This suggests that the lateral diffusions is about a factor 2 slower than in the vertical direction. The damage visible to the InGaAs contact layer is a result of the stain etch and not related to the diffusion process.

This experiment confirms, that the diffused doping profile can be optimized to meet the requirements of standard foundry processes.

4. Characterization

In order to verify the simulations, test structures as shown in Fig. 5 were fabricated based on waveguides as shown in Fig. 1 with a 600 nm thick Q(1.25) guiding layer. The p-dopant was introduced locally as described above, with a diffusion depth of 1.63 μm.

4.1. Zn-diffused waveguide array

The test structure shown in Fig. 5(a) is based on shallow etched waveguides, routed through p-doped regions of different length L_{Dif}. The average absorption coefficient of each waveguide can be written as the sum of the absorption coefficient in the n and p-doped regions, α_n and α_p, as :

$$\alpha = \alpha_n + \Lambda\alpha_p + \alpha_s \tag{1}$$

where $\Lambda = L_{Dif}/L$ is the ratio between the length of the diffused region, L is the total waveguide length and α_s the scattering loss. The loss of each individual waveguide is derived from the Fabry-Perot method, with [20]:

$$\alpha L = ln(\frac{1}{R}\frac{\sqrt{\gamma}-1}{\sqrt{\gamma}+1}) \tag{2}$$

where γ is the ratio between maximum and minimum transmission and R is the power reflection coefficient. Consequently, we can measure the loss contributions independently with:

$$\alpha(\Lambda = 0) = \alpha_n + \alpha_s \tag{3}$$

and

$$\alpha(\Lambda_1) - \alpha(\Lambda_2) = \alpha_p(\Lambda_1 - \Lambda_2) = \frac{1}{L}ln(\frac{\sqrt{\gamma_1}-1}{\sqrt{\gamma_1}+1}\frac{\sqrt{\gamma_2}+1}{\sqrt{\gamma_2}-1}) \tag{4}$$

where the indices correspond to the nth waveguide of the array. According to above definitions, the method introduces an uncertainty for $\alpha(\Lambda = 0)$, since it relies on an estimate of the facet reflectivity. α_p is derived however independently of the reflection coefficient.

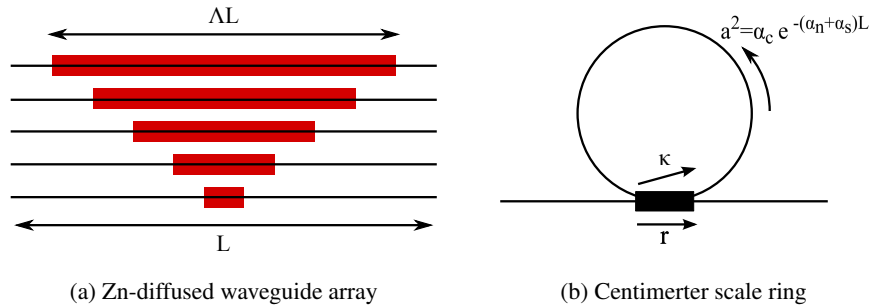(a) Zn-diffused waveguide array   (b) Centimerter scale ring

Fig. 5. Test structures for characterization of the waveguide loss.

The experiment contains an array as displayed in Fig. 5(a) with six shallow waveguides of 14.2 mm length. Five of the waveguides are routed through areas which were exposed to the diffusion process. The width of the diffusion areas is maintained constant at 30 μm, while the length is altered from 1.4 mm to 12.4 mm. The pitch between the diffusion areas is approximately 75 μm and the ratio Λ is varied from 0 to 0.85.

The loss is measured with a tunable laser, where the lasing wavelength has been altered from 1540 nm to 1550 nm with a step size of 0.1 pm. The transmission spectrum of each waveguide is recorded with a power meter and a peak detection algorithm is applied to find approximately 440 minima and maxima of the transmission spectrum. These values are used to calculate the uncertainty of each measurement. The reflection coefficient was calculated for both polarizations and estimated to be 0.34 for TE and 0.28 for TM respectively.

The result for TE is displayed in Fig. 6(a) and fit to a linear equation, where according to Eqs. (3) and (4), the slope defines the p-dopant contribution and the value at Λ=0 is the n-dopant contribution. Consequently, we find a propagation loss of 0.3 dB/cm $\pm$ 0.1 dB/cm and 2.0 dB/cm $\pm$ 0.1 dB/cm for not p-doped and p-doped waveguides respectively. A similar graph is shown in Fig. 6(b) for TM, with a propagation loss of 0.4 dB/cm $\pm$ 0.1 dB/cm and 2.2 dB/cm $\pm$ 0.1 dB/cm respectively. These results show excellent agreement with the simulated values listed in Table 1 for a 600 nm thick guiding layer. The slightly higher value measured for the p-doped waveguides can be explained by a 30 nm smaller distance between guiding layer and doping front.

Further measurements were performed on deep etched waveguides which did not contain p-dopant. Values of 1.4 dB/cm $\pm$ 0.2 dB/cm for TE and 2 dB/cm $\pm$ 0.2 dB/cm for TM are in good agreement with predictions.

4.2. Ring resonator

To verify the low loss of the not p-doped shallow waveguides we used a second test structure based on a all-pass ring resonator, which has been extensively described for various material platforms [21–23]. Recently this ring resonator has been applied for the measurement of optical loss [9]. In this work, we increase the measurement sensitivity by increasing the ring circumference from a few millimeter to several centimeter.

4.2.1. Ring resonator design

A ring resonator, as shown in Fig. 5(b), consists of a circular optical waveguide cavity, which is accessed via a coupling element. Light that enters the cavity interferes constructively after one round trip L if the round trip phase $\phi = \beta L$ equals an integer multiple of 2π.

This results in a periodic transmission, with a free spectral range $FSR = \lambda^2/(n_g L)$. Under
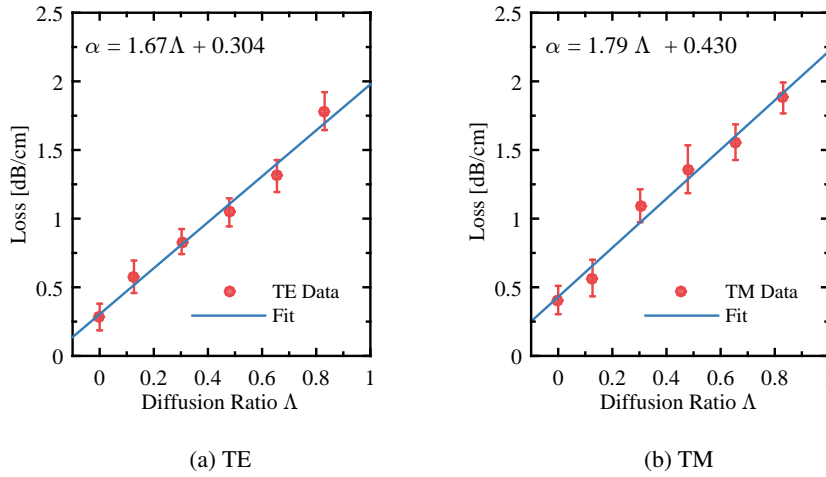
(a) TE (b) TM

Fig. 6. Measured waveguides of fixed length which are guided through diffusion areas of different length. The solid line represents a fit to the measurement with the result given as inset.

the assumption that the back reflections of the coupling element can be neglected, the power transmission of the ring resonator can be written as:

$$T = \frac{a^2 - 2racos(\phi) + r^2}{1 - 2racos(\phi) + (ra^2)} \tag{5}$$

where the bar coupling is described by the coefficient r, which in the ideal case is related to the cross coupling coefficient via $r^2 + \kappa^2 = 1$. The round trip transmission of the resonator is a^2 and includes coupling element α_c and the ring waveguide $e^{-(\alpha_s + \alpha_n)L}$:

$$a^2 = \alpha_c e^{-(\alpha_s + \alpha_n)L} \tag{6}$$

The similarity of denominator and numerator suggests, that for an ideal structure with no insertion loss, i.e. $a = 1$, the transmission is always unity. For $r = a$, the transmission drops to zero, which is defined as critical coupling. The extinction ratio for the general case, follows directly for the conditions of $cos(\phi) = 1$ or $cos(\phi) = -1$ and can be written as:

$$ER = \frac{T_{max}}{T_{min}} = \frac{(a+r)^2}{(1+ra)^2} \frac{(1-ra)^2}{(a-r)^2} \tag{7}$$

For a fixed coupling geometry, the waveguide loss of the ring waveguide can be calculated using Eq. (7) or fitting the equation to measurements of rings with different circumference. Once the round trip transmission a^2 is obtained, the absorption coefficient can be derived from:

$$\alpha = -\frac{1}{L} ln(\frac{a^2}{\alpha_c}) \tag{8}$$

The ER is plotted in Fig. 7(a) against the waveguide loss for a 5 cm ring with various coupling coefficients. The ER changes rapidly with a maximum sensitivity near the critical coupling point. When estimating the propagation loss, it is thus convenient to choose a set of rings which operate close to the critical coupling point. For the experimentally obtained waveguide loss of

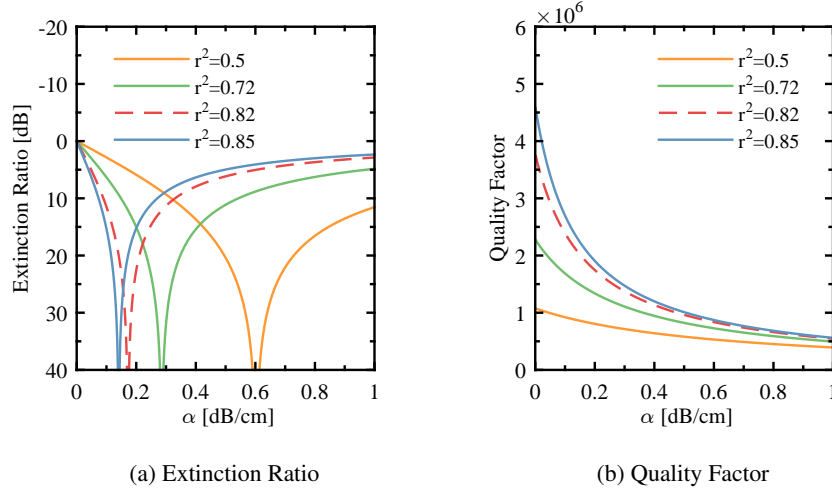(a) Extinction Ratio

(b) Quality Factor

Fig. 7. Simulations for different coupling coefficients and a ring circumference of 5 cm.

approximately 0.3 dB/cm, a coupling coefficient of 0.72 is a good choice for this resonator length.

The uncertainty of the coupler transmission α_c is independent of the round trip transmission and can be estimated by measuring two rings with a different circumference. The error introduced for a wrong estimate, compared to the reference α_{co} is derived directly from Eq. (8) as:

$$\Delta\alpha = -\frac{1}{L}ln(\frac{\alpha_c}{\alpha_{co}}) \tag{9}$$

Thus an error of 0.1 dB in the extinction ratio, leads to an uncertainty of 0.1 dB/cm in the propagation loss for a circumference of 1 cm.

Furthermore, the deviation from the nominal coupling coefficient r_0 introduces an error in the estimated round trip transmission. Under the assumption that the ring is used near the critical coupling point, the error is approximated by calculating the shift in the critical coupling condition via:

$$\Delta\alpha \approx -\frac{2}{L}ln(\frac{r}{r_o}) \tag{10}$$

The shift in critical coupling can be estimated in Fig. 7(a) from the dashed curve, which implies a shift of 3% with respect to the nominal coupling coefficient of 0.85. With a length of 5 cm, the error is only a few 0.01 dB/cm. Alternatively the quality factor of the rings can be measured, which is defined as the resonance wavelength divided by the width of the resonance peak:

$$Q = \frac{\lambda_0}{\Delta\lambda} = \frac{\pi n_g L\sqrt{ra}}{\lambda_0(1-ra)} \tag{11}$$

where $\Delta\lambda$ describes the Full-Width Half Maximum (FWHM) of the resonance and n_g the waveguide group index. This quantity is a measure for the detection limit of a sensing systems and will be measured to back up the results obtained from the ER method. The dependence on Q for different values of the propagation loss is shown in Fig. 7(b). For the example of 5 cm circumference, the ER is larger than 10 dB and the Q is approximately one million.
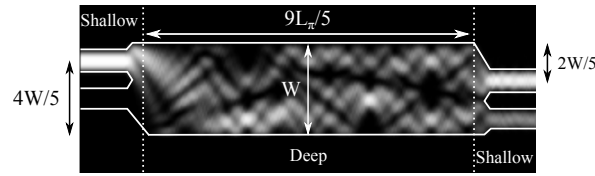
Fig. 8. Simulation of an MMI-coupler with r^2=0.72. The access waveguides are shallow and the multimode region is deeply etched.

4.2.2. Multimode interference devices

MMIs are an ideal choice for our application, since they provide a high fabrication tolerance and low insertion loss [24]. The device relies on the excitation of a set of modes inside a multimode waveguide, which propagate and interfere constructively at the imaging length, to form a self or split image at the output. This can be seen in Fig. 8, where we display the numerical simulation of the propagation inside the multimode section for a device with two inputs and outputs. In the presented case, the upper input is excited. The device length of $L = 3NL_\pi/5$, is chosen according to existing analytical solutions [25], to produce an asymmetric splitting ratio. L_π is a geometrical constant which describes the beat length of the two lowest order modes with a difference in propagation constants $\Delta\beta$, and is defined as $L_\pi = \frac{\pi}{\Delta\beta} \approx \frac{4n_r W^2}{3\lambda_0}$, where W and n_r are the width and effective refractive index of the multimode ridge. With $N = 3$ and access waveguides positioned as described in Fig. 8, a coupling coefficient of $r^2 = 0.72$ is expected, which matches the design value derived in the simulation section above. Reflections at the facets of the MMI are reduced by using shallow etched access waveguides and tilting the facets of the MMI by 54 degree. The shallow waveguides introduce some coupling at the input of the MMI, which causes additional imbalance at the output through interference. From simulations, an 11 μm wide multimode section is needed to avoid this, resulting in a length of 512 μm.

The measurement of insertion loss and coupling coefficients is enabled by placing two couplers between reflective facets as displayed in Fig. 9(a). The MMIs are fabricated in close proximity and the input for both structures is maintained the same, while the output port is varied. The ports that are not of interest for the measurement are curved and terminated, such that the light exits the coupler and does not contribute to the measured signal. For this structure the Fabry-Perot Method (Eq. (2)) can be used to measure the transmission coefficient of the MMI.
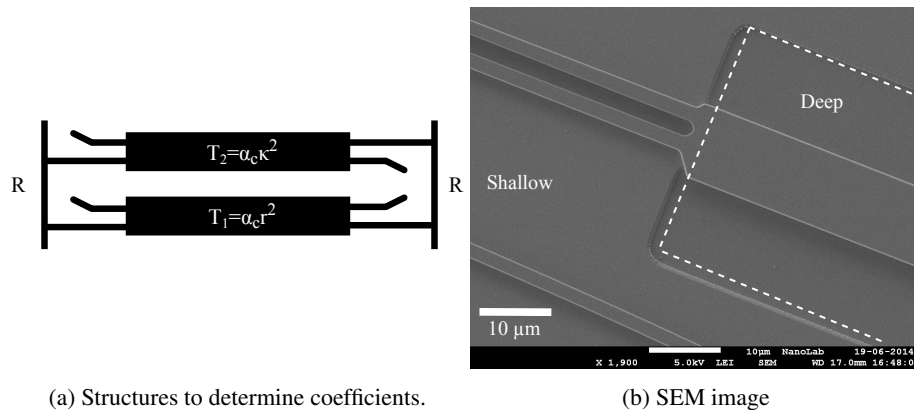
(a) Structures to determine coefficients.

(b) SEM image

Fig. 9. MMI coupling element.

The coupling coefficients r^2 and κ^2 can be directly derived from these transmission values. The uncertainty in the waveguide loss and the coupler insertion loss is removed with the following normalization:

$$r^2 = T_1/(T_1 + T_2) \qquad \kappa^2 = T_2/(T_1 + T_2) \tag{12}$$

with $r^2 + k^2 = 1$. T_1 and T_2 represent the measured bar and cross transmission of the coupling element. The insertion loss for both structures is displayed in Fig. 10(a) for TE where the background waveguide loss is subtracted. The solid lines represent the simulations of the corresponding port assuming a 250 nm deviation from the nominal MMI width of 11 μm. This deviation was verified using SEM cross-section images. The excellent agreement, suggests that the central wavelength of the MMI has shifted by about 40 nm, to 1510 nm. The estimated insertion loss at 1510 nm is 0.1 $\pm$0.1 dB. The experiment has been repeated for TM, as displayed in Fig. 10(b). The central wavelength is at 1540 nm, which agrees with the simulations as well.

The corresponding coupling coefficients have been extracted from these measurements and
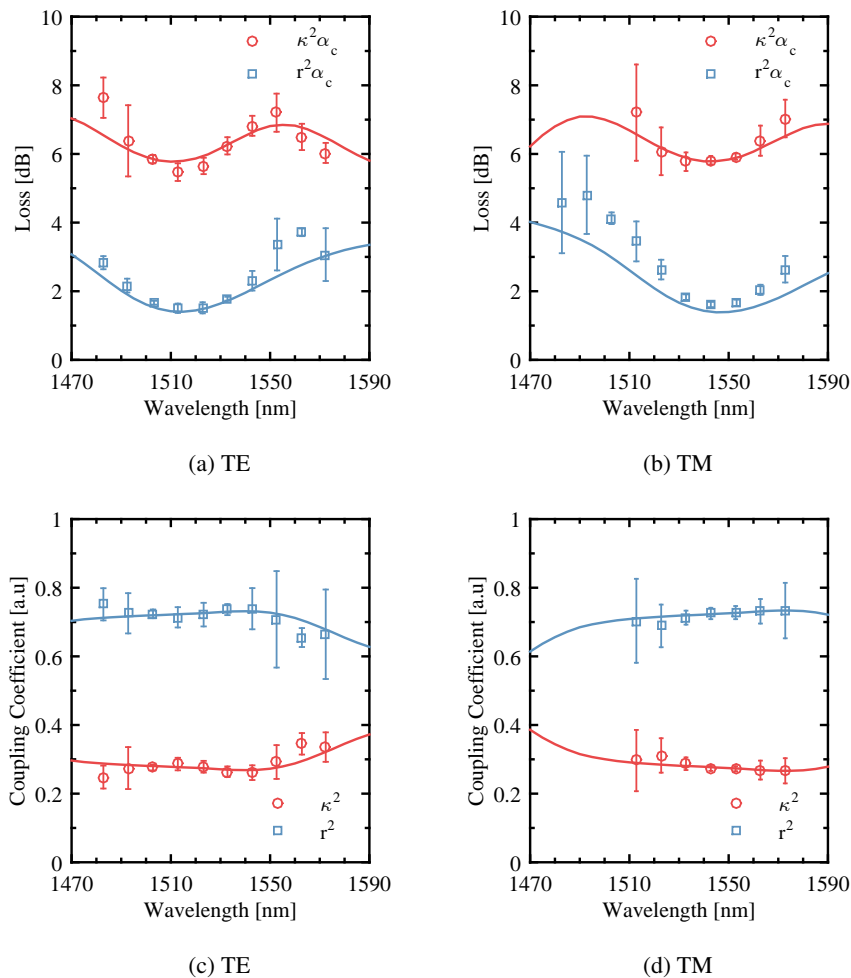

(a) TE

(b) TM

(c) TE

(d) TM

Fig. 10. Transmission and coupling coefficients of the MMI-coupler. Solid lines represent BPM simulations for a 10.75 μm wide coupler.

Eq. (12). The result for TE is shown in Fig. 10(c) together with the simulation in solid. The good agreement suggests, that $r^2=0.72 \pm 0.02$ is achieved at the point of minimum insertion loss. A similar result is obtained for TM, as shown in Fig. 10(d). Consequently, the experiment suggests that the ring resonators based on this component should perform close to ideal around 1510 nm for TE and 1540 nm for TM.

Spatial modefilter

The suppression of the first order mode is of importance to avoid inter-modal interference, which causes a shift of the coupling parameters. An excitation of the first order mode can be achieved by a misalignment of the input stage with respect to the circuit waveguide [26] or irregularities in the waveguide. Consequently, according to Eq. (10), the accuracy of the measurement depends on the experimental alignment, hampering the reproducibility.

For this purpose MMIs can be designed to act as filter which spatially separate the waveguide modes. The simplest method is to use a MMI with one input and one output, as depicted in Fig. 11(a). The length of the device is $L = 3L_\pi/4$. The access sidewall of the MMI is shallow and angled at 54 degree to reduce back reflections.

As seen in Fig. 11(a) the fundamental mode is transmitted without penalty, while the first order mode shown in Fig. 11(b) is imaged onto the MMI access sidewall. This spatial separation results in a significant insertion loss for the first order mode. The transmission of the device is simulated for a number of device widths and shown in Fig. 11(c) for the fundamental and in Fig. 11(d) for the first order mode.

From the simulations, we chose a 10 μm wide and 213 μm long device. With a suppression of 30 dB over a wide wavelength range, the device guarantees negligible deviation form the

(a) BPM fundamental

(b) BPM first order

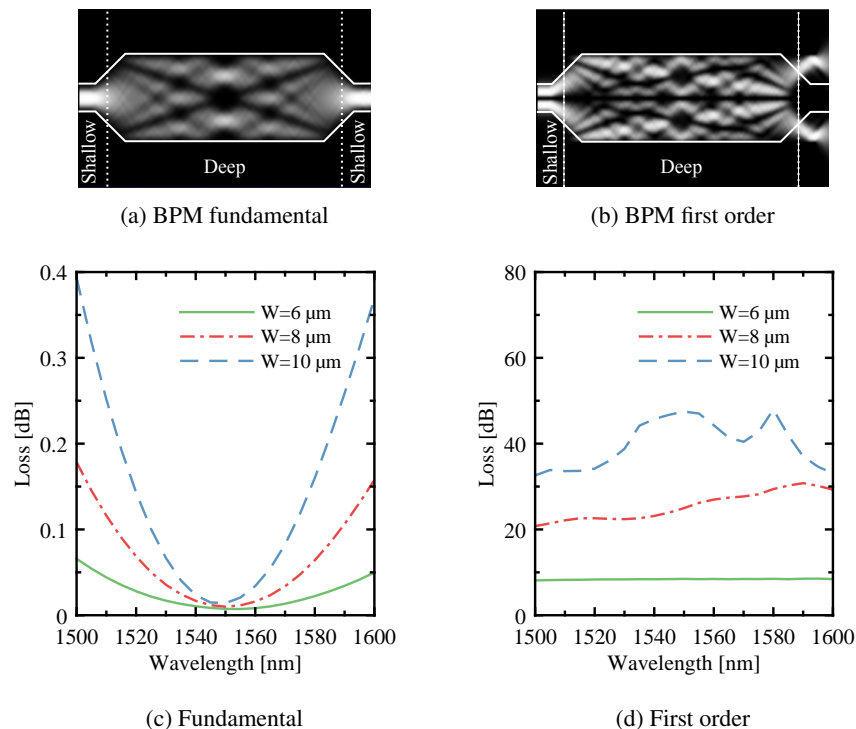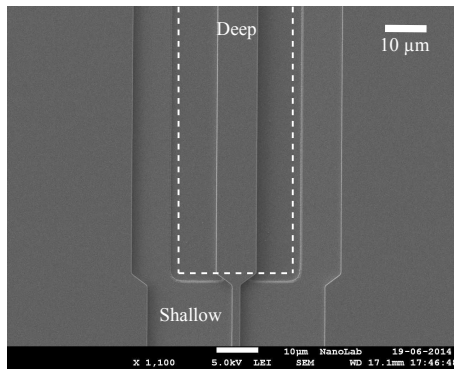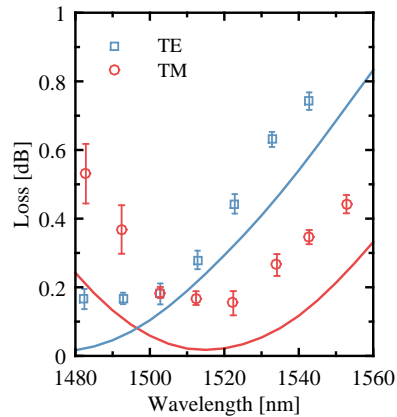(c) Fundamental

(d) First order

Fig. 11. BPM simulation of modefilter for different propagation modes.

(a) SEM of spatial modefilter

(b) Measurements for first order mode

Fig. 12. Spatial modefilter. Solid lines represent simulated loss for a 9.75 μm wide MMI.

nominal coupling coefficients.

The characterization of this component has been undertaken by concatenating up to 16 devices in a row. The loss is again measured by using the Fabry-Perot method (Eq. (2)). The result for TE and TM is shown in Fig. 12(b), compared to simulations of the device with the 250 nm deviation from the nominal MMI width of 10 μm. The minimum insertion loss of the device is found to have shifted more than for the coupling element, to 1480 nm and 1520 nm for TE and TM respectively. This was not anticipated in the design, and is caused by the difference in nominal width of the two MMI elements. However, due to the larger bandwidth of this device, the modefilter will account for approximately 0.3 dB insertion loss at 1510 nm and 1540 nm for TE and TM respectively.

4.2.3. Optical characterization

In this section the transmission spectrum of the ring resonator based on a not p-doped shallow etched spiral is discussed. The circuit was fabricated with the MMI components as described and characterized above. Due to the large length required for a high resolution measurement, the ring geometry will have a large footprint. This can be overcome using a spiral ring resonator, as shown in Fig. 13 for a circumference of 73 mm. The outer radius of the spiral is slightly larger than 1 mm and the inner radius is approximately 0.5 mm. The number of waveguide junctions is minimized by a gradual reduction of the radius towards the center of the spiral. The total footprint of the device is 2.5 mm x 3.5 mm, mainly determined by the two inner bends. The optical ports are formed by 7 degree angled cleaved waveguide facets. The pitch of the spiral is 25 μm. Spatial modefilters are placed at the optical ports and inside the ring to avoid excitation of higher order modes. Rings with circumferences of 25 mm, 55 mm and 73 mm were fabricated.

For the characterization of the resonators, the setup depicted in Fig. 13 is chosen. A tunable laser is coupled via a collimating lens to free space. After passing through a polarizer, the collimated beam is coupled to the device via a microscope objective. A fiberized polarization controller is used to maximize the transmission through the polarizer set to TE or TM.

The FSR of the devices is expected to be in the order of a few picometer. A transmission experiment using a tunable laser in step mode thus requires a step, which is hundreds times
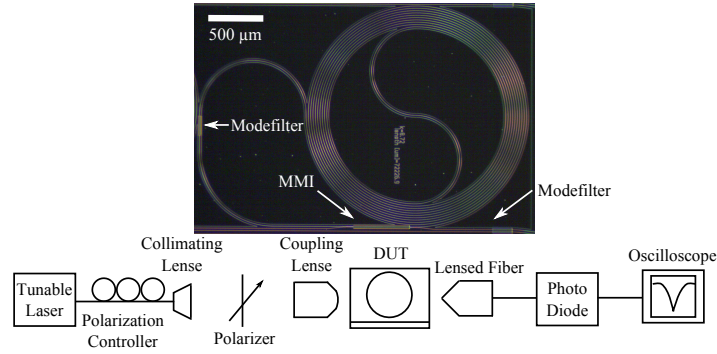
Fig. 13. Characterization setup for a fabricated ring resonator. The spiral of the ring is etched shallow, while MMI and modefilter are deep.

smaller to avoid sampling errors. Therefore, the laser is operated in continuous sweep mode at a fixed tuning speed. By using a real-time oscilloscope to sample the recorded transmission signal, a high resolution is obtained.

The resolution of the measurement is determined by the oscilloscope's sampling frequency of 100 kHz, and the laser sweep speed of 500 pm/s, resulting in a step size of 5 fm. The lasing wavelength was chosen as 1510 nm for TE and 1540 nm for TM, in agreement with the MMI characterization discussed above. Three rings with a circumference of 25 mm, 55 mm and 73 mm were characterized. From the transmission spectra, the FSR of the rings was found to be 8.2 pm, 11.9 pm and 24.1 pm for TE and 9.0 pm, 12.4 pm and 25.3 pm for TM polarization. The transmission spectra were separated in FSRs and each period fit to the analytical ring transmission to obtain the ER and the Q. A typical fit for the device with 73 mm circumference is given in Fig. 14(a) for TE and Fig. 14(b) for TM.

The experiment was repeated for all rings. The estimate for the insertion loss of the MMI coupler and the modefilter was 0.4 dB. The result for the ER is given in Fig. 15(a) and suggests
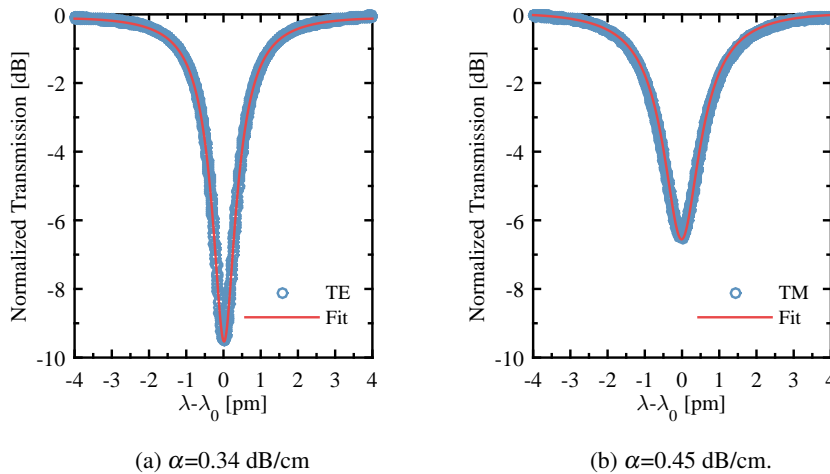

(a) α=0.34 dB/cm

(b) α=0.45 dB/cm.

Fig. 14. Transmission of ring resonator with 73 mm circumference. The derived insertion loss from the fit is given in the caption based on the assumption of α_c=0.4 dB for both MMIs.
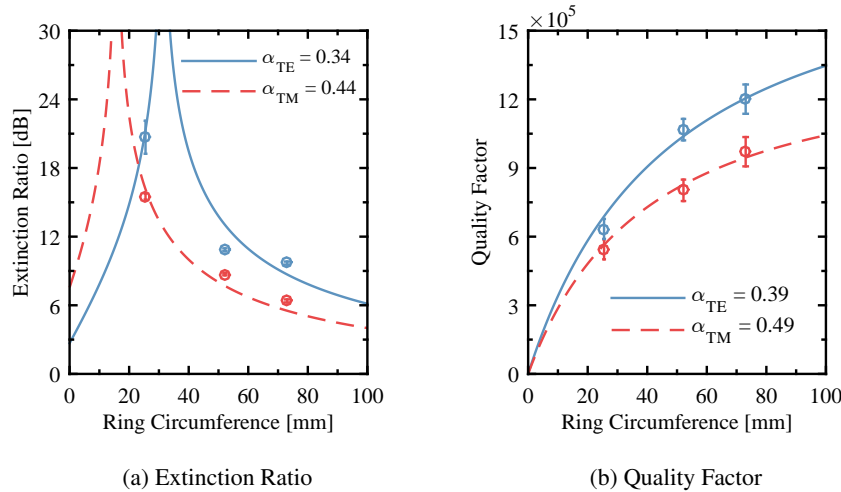
(a) Extinction Ratio

(b) Quality Factor

Fig. 15. Measurement of ring resonators with different circumference. The lines represent fits to analytical equations, with the derived insertion loss given in the legends . Starting guess for α_c was 0.4 dB which includes both MMIs.

an insertion loss of 0.34 dB/cm for TE and 0.44 dB/cm for TM. This is in agreement with the results obtained from the waveguide array and is an excellent match with the simulation values in Table 1.

This result is backed up with the measurement of the quality factor as displayed in Fig. 15(b). The fit in this case is obtained for TE with 0.39 dB/cm and 0.49 dB/cm for TM, which agrees well with the results obtained from the *ER* method.

The values obtained for the longest ring, suggest a record quality factor for an InP ring, suitable for fabrication of high performance angular velocity sensors [4] within an InP generic foundry process.

5. Conclusion

This paper describes the development of a Zn-diffusion step within a generic integration process, to restrict the absorbing p-dopant to the regions where a p-n junction is required and thus avoid dopant in transparent waveguide regions. The loss in the passive waveguides is reduced from 2 dB/cm to 0.4 dB/cm and is in excellent agreement with our simulations. The low loss was confirmed by fabrication and characterization of a spiral ring resonator with a circumference of 73 mm. A record quality factor of 1.2 million with an extinction close to 10 dB is measured in TE polarization. This value increases the state of the art by about 20% and is an important step towards generic PICs for demanding sensing applications.

Acknowledgments